Supplementary Information for:

Insights into IgM-mediated complement activation based on *in situ* structures of IgM-C1-C4b

Thomas H. Sharp[1,*], Aimee L. Boyle[2], Christoph A. Diebolder[3], Alexander Kros[2], Abraham J. Koster[1] and Piet Gros[4]

[1]Section Electron Microscopy, Department of Cell and Chemical Biology, Leiden University Medical Center, 2300 RC Leiden, The Netherlands

[2]Leiden Institute of Chemistry, Gorlaeus Laboratories, Leiden University, 2333 CC Leiden, The Netherlands

[3]NeCEN, Gorlaeus Laboratories, Leiden University, 2333 CC Leiden, The Netherlands

[4]Crystal and Structural Chemistry, Bijvoet Center for Biomolecular Research, Faculty of Science, Utrecht University, Padualaan 8, 3584 CH Utrecht, The Netherlands

Correspondence to: t.sharp@lumc.nl

This PDF file includes:

Supplementary Materials and Methods

Peptide synthesis

Fmoc-protected amino acids, Rink amide resin, and (O-1H-6-cholorobenzotriazole-1-yl)-1,1,3,3-tetramethyluronium hexafluorophosphate (HCTU) were purchased from NovaBioChem (Amsterdam, Netherlands). Dimethylformamide (DMF), N,N-diisopropylethylamine (DIPEA), piperidine, diethyl ether, acetonitrile (MeCN), and trifluoroacetic acid (TFA) were purchased from Biosolve (Valkenswaard, Netherlands). Triisopropylsilane (TIPS), dichloromethane (DCM), and cholesteryl hemisuccinate were purchased from Sigma Aldrich (Zwijndrecht, Netherlands). Fmoc-NH-(PEG)4-COOH was purchased from Iris Biotech (Marktredwitz, Germany).

A CD52 mimotope with the amino-acid sequence TSSPSAD was synthesized by solid-phase peptide synthesis using a CEM Liberty 1 microwave-assisted peptide synthesizer (CEM Coporation, North Carolina, USA), with a Rink amide resin employed as the solid support. Fmoc-deprotections were facilitated using 20% piperidine in DMF (v/v) and amino acid couplings were performed using HCTU as the activator and DIPEA as base. After synthesis of the peptide, Fmoc-NH-(PEG)4-COOH (1.2 equivalents) was manually coupled to the N-terminus of the peptide using HCTU (3 equivalents) and DIPEA (4 equivalents) in DMF. Fmoc deprotection of the PEG linker was achieved, after 16 hours coupling, using a solution of 20% piperidine in DMF (v/v) before cholesteryl hemisuccinate (2 equivalents) was coupled using HCTU (3 equivalents) and DIPEA (4 equivalents) in DMF. After overnight coupling of the cholesteryl hemisuccinate, the resin was washed with DMF and DCM before cleavage of the cholesterol-PEG-peptide conjugate was facilitated with a TFA:TIPS (95:5 v/v) mixture. After 1 hour, the cleaved peptide was precipitated into ice-cold diethyl ether, the precipitate was collected by centrifugation, redissolved in a mixture of water:MeCN (4:1 v/v), and freeze-dried.

Purification of the peptide was performed by reversed-phase HPLC (high-performance liquid chromatography) using a Shimadzu HPLC system with two LC-8A pumps and an SPD-10AVP UV-Vis detector (Shimadzu Benelux, ‘s-Hertogenbosch, Netherlands). Samples were eluted

from a Vydac C4 reversed-phase preparative column running a gradient from 10 – 90 % B (where A is 1% TFA in H2O and B is 1% TFA in MeCN) at a flow rate of 15 ml/min. The identity and purity of the collected fractions was assessed by liquid chromatography-mass spectrometry (LC-MS) using a Thermo Scientific Ultimate 3000 LC system paired with a Thermo Scientific TSQ Quantum Access Max triple quadrupole mass spectrometer (ThermoFisher Scientific, Netherlands). Fractions containing peptide of the correct mass and >95% purity were pooled and freeze-dried before use.

Liposome formation

Dimyristoylphosphatidylcholine (DMPC), dimyristoylphosphatidylglycerol (DMPG), and cholesterol were purchased from Avanti Polar Lipids (Alabama, USA). Lipid films composed of DMPC:DMPG:cholesterol:CD52-cholesterol (45:5:49:1 mol%) were formed by dissolving the components in chloroform:methanol (9:1 v/v) before drying under nitrogen gas and desiccation for 2 hours. Films were rehydrated at 37°C for 30 minutes with 20 mM sulforhodamine B (S1402 from Sigma Aldrich, Missouri, USA) in phosphate-buffered saline (PBS), pH 7.4, to a concentration of 0.8 mg/ml. Liposomes were formed by sonication for 5 minutes at 37°C in a water bath and purified by size-exclusion chromatography using a prepacked NAP-25 column (17-0852-01 from GE Healthcare, Little Chalfont, UK).

Complement activation fluorescence assay

Monoclonal anti-CD52 IgM (clone YTH66.9HL) was purchased from Bio-Rad (Veenendaal, Netherlands). NHS was purchased from Complement Technologies (Tyler, TX, USA). Fluorescence of sulforhodamine B was monitored using a CLARIOstar microplate reader (BMG Labtech, Offenburg, Germany) with an excitation wavelength of 565 nm and emission wavelength of 585 nm. To assess complement activity, purified liposomes were diluted 20× with PBS before NHS and IgM were added to final concentrations of 10% (v/v) and 10 µg/ml, respectively. To evaluate the effect of temperature on complement activity, purified liposomes (diluted 20× with PBS) and IgM (10 µg/ml final concentration) were mixed at 21°C for 20 min before being cooled on ice for 20 min. Next, ice-cold NHS (10% v/v final concentration) was added. Samples were stored on ice until analysis, when they were

inserted into the plate reader at the time-points indicated and allowed to warm to 21°C during data collection.

Sample preparation for cryo-electron tomography

Undiluted liposomes were mixed with IgM (0.1 mg/ml final concentration) and incubated at room temperature for 20 minutes. To form IgM-C1 complexes, samples were then cooled to 4°C for 20 min before NHS (10% v/v final concentration) was added and incubated at 4°C for a further 20 min before vitrification. Ice-cold bovine serum albumin-coated 10 nm gold colloids (Cell Microscopy Core, Utrecht University, Utrecht, The Netherlands) were added as fiducials. Samples were pipetted onto freshly plasma-cleaned 300 mesh copper grids with lacey-carbon support (Electron Microscopy Sciences, PA, USA) and vitrified in liquid ethane using a Leica EMGP (Leica Microsystems, Wetzlar, Germany) cooled to 4°C.

Cryo-electron tomography data collection

Grids were loaded into a Titan Krios transmission electron microscope (Thermo Fisher Scientific, Hillsboro, OR, USA) equipped with a field emission gun operating at 300 kV and a Volta phase plate (Thermo Fisher Scientific) heated to 225°C. Zero-energy-loss images were acquired using a GIF-Quantum LS energy filter (Gatan, Pleasanton, CA, USA), with a slit width of 20 eV, on a K2 Summit direct electron detector (Gatan) operating in counting mode. Tilt series were collected in batch mode using the software program Tomography 4.0 (Thermo Fisher Scientific) at ×33,000 magnification using a discontinuous tilt scheme from 0° to −54° before collecting 0° to +54°, in 2° increments. Exposures of 2.4 sec were dose-fractionated into 6 movie frames per tilt angle. The total dose for each tilt series was 80 $e^{-}/Å^{2}$. Focusing to −300 nm was performed before each image acquisition using a low-dose routine. Before each tilt series, the Volta phase plate was advanced to a new area, allowed to settle for 300 sec, and then conditioned for 80 sec to generate an approximate phase shift of 90° (1). The phase plate was also conditioned for an additional 5 sec between every fifth image.

Tomogram reconstruction and subtomogram averaging

Raw frames were aligned using "alignframes" from the software program IMOD (2), and tomograms were reconstructed using weighted back-projection with IMOD (2). Particles of IgM-C1 complexes were then manually picked from 54 tomograms using e2spt_boxer.py from the software program EMAN2 (3), yielding 1,522 particles that were extracted with a box size of 160 pixels and a final pixel size of 4.3 Å/pixel. During extraction, contrast was inverted and particle density normalized. An initial model of the IgM-C1 complex was created by aligning 1,024 particles using e2spt_binarytree.py (3) (**SI Appendix, Fig. S3**). All particles were aligned to the initial model using global alignment parameters in Dynamo (4). Following coarse alignment, the resulting map was used as a reference for classification in Dynamo using multireference alignment. White noise was added to six copies of the reference using EMAN2 and each copy was low-pass filtered to 60 Å before particles were aligned using a refined orientation search in Dynamo (4): Initially, search parameters allowed a 60° tilt away from the z axis (perpendicular to the membrane) and a full 360° rotation around the z axis. Search parameters for later iterations were further constrained. The resulting 3 best classes corresponded to a hexameric IgM-C1-C4b$_2$ complex, a pentameric IgM-C1-C4b$_2$ complex and a pentameric IgM-C1-C4b$_1$ complex (**SI Appendix, Fig. S3**). Other classes could not be refined to higher resolution. Individual even/odd gold-standard refinements was performed for each class. To perform even/odd gold-standard refinements, white noise was added to 3 low-pass filtered copies of the original reference and even/odd particle stacks were generated using the particles that contributed to each class. Individual refinements were performed using the same search parameters as described above. To generate the C6-symmetric map, after even/odd-refinement a cylindrical mask was applied around the Fc-platform of the hexameric IgM-C1-C4b2 complex, and C6-symmetry applied to both even and odd halves. FSC curves were generated from tightly-masked volumes using EMAN2 (3). Resolutions reported are at FSC = 0.143 (**SI Appendix, Fig. S3**).

Model building

To create a model of the IgM-Fc platform, we used the C6 symmetric map of the hexameric IgM-C1-C4b$_2$ complex. Following previous constructions of soluble IgM models (5, 6), a Cε3-4/Cε3'-4' dimer of IgE-Fc (pdb code 1O0V) (7) was fitted into the density of the planar Fc

platform, yielding a ring of six Fc regions. The Cε4/4' dimer was exchanged for the crystal structure of the Cμ4/4' dimer (5) (pdb code 4JVW) and the fit optimized using the 'fit in map' command from UCSF Chimera (8). Each Cε3 domain was exchanged for the Cμ3 NMR structure (5) (pdb code 4BA8) and the fits individually optimized using 'fit in map'. A Cμ2/Cμ2' dimer (5) (pdb code 4JVU) was fitted into the map of the hexameric IgM-C1-C4b$_2$ complex at an obtuse angle of ca. 100° with respect to the Fc Cμ3-4/Cμ3'-4' domains. Below Cμ2/Cμ2', the Fab domains (9) (pdb code 1DEE) fit the complex with C6 symmetry. C6 symmetry was broken for both Fab2 adjacent to the two C4b, which were moved up to ~2.5 nm away from C4b to better fit the density and also remove steric clashes with C4b-MG1 and MG5 domains. To create models for pentameric IgM in IgM-C1-C4b$_1$ and IgM-C1-C4b$_2$, one protomer consisting of one Fc (Cμ3-4/Cμ3'-4'), one dimeric hinge domain (Cμ2/Cμ2') and Fab2 arms was removed from hexameric IgM. For pentameric IgM-C1-C4b$_1$ only the Fab2 adjacent to the single C4b was displaced from its C6 symmetric position.

To construct a model of C1q, the collagen-like arms of C1q were modelled using ccbuilder 2.0 (10) with a radius of 3 Å and a pitch of 60 Å. Each collagen arm was split into three sections, comprising a stalk (res. A1-39, B1-41, C1-38), linker (A40-57, B42-59, C39-56) and lysine-containing segment (A58-87, B60-89, C57-86). Each segment was fitted into the map manually the fit optimized using the 'fit in map' command from UCSF Chimera (8). C1q head domains (11) (pdb code 1PK6) were manually placed and C6 symmetry applied before each was optimized using 'fit in map' without allowing rotation.

The C1rs CUB1-EGF-CUB2 platform was modelled based on a single C1rs heterodimer (chains A and B) from the crystal structure of the C1rs heterotetramer (12) (pdb code 6F1C). CUB2 from C1s was fitted independently into the map and the remainder of the CUB1-EGF-CUB2 platform placed and optimized using 'fit in map'. C1r CCP1-CCP2-SP domains were taken from 1GPZ (13), which were manually placed and optimized using 'fit in map'. C1s CCP1-CCP2-SP domains were taken from 4J1Y (14). To fit C1s, first the structure of MASP2 in complex with C4 (15) (pdb code 4FXG) was placed in the density to ensure correct orientation of the SP domain, before MASP-2 was replaced with C1s and the fit optimized using 'fit in map' without allowing rotation. C4b (16) (pdb code 5JTW) was manually placed and the fit optimized using 'fit in map' (8). The structures used for the final models are summarized in **SI Appendix, Table S1**.

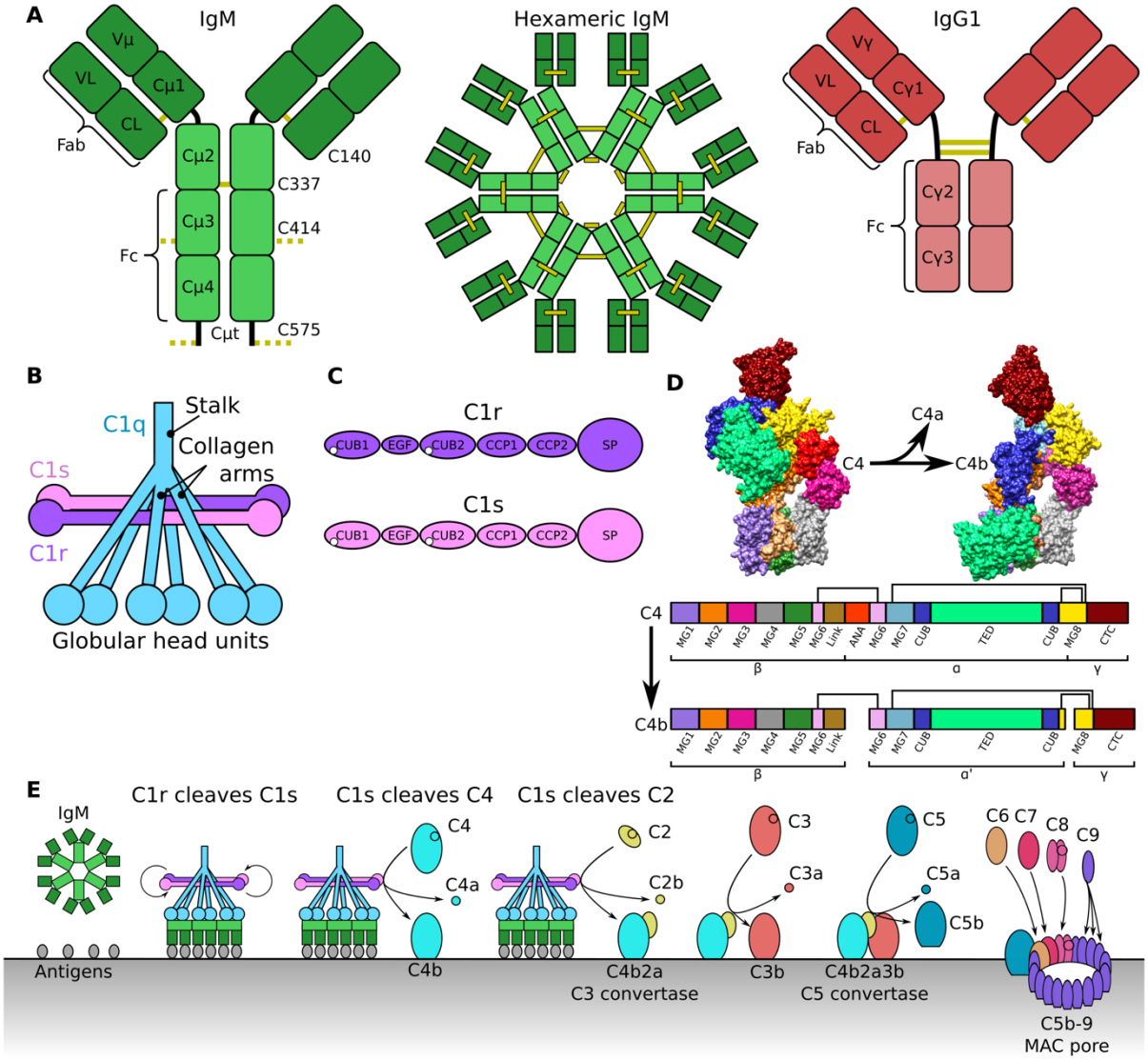

Fig. S1. Schematic diagrams of antibody complexes, C1q, r, and s, and C4b.

A) Domain layouts for an IgM protomer (*left*), a hexameric IgM complex (*middle*), and monomeric IgG1 (*right*). Disulfides mediating antibody formation and oligomerisation are numbered and shown as yellow lines. Heavy-chain domains for IgM and IgG are denoted μ and γ, respectively, and light chains denoted as 'L'. Constant and variable domains are denoted C and V, resp. **B)** Schematic diagram of the $C1qr_2s_2$ complex. C1q (blue) encapsulates a heterotetramer of 2 × C1r (purple) and 2 × C1s (pink). C1q comprises a stalk domain and 6 (heterotrimeric) collagen arms that terminate with (heterotrimeric) globular head units. **C)** Domain layouts for C1r (purple) and C1s (pink). Calcium ions mediating C1q binding are shown as white circles/spheres. Abbreviations: CUB, 'Complement C1r/C1s, Uegf, Bmp1'; EGF, epidermal-growth factor; CCP, complement-control protein; SP, serine protease. **D)** Surface representation of the crystal structures of C4 (15) and C4b (17) (pdb codes 4FXG and 5JTW, resp.). Abbreviations: MG, macroglobulin; TED, thioester-containing domain; CTC, C-terminal C345c domain; ANA, anaphylatoxin domain. **E)** Reaction schematic for the classical complement pathway.

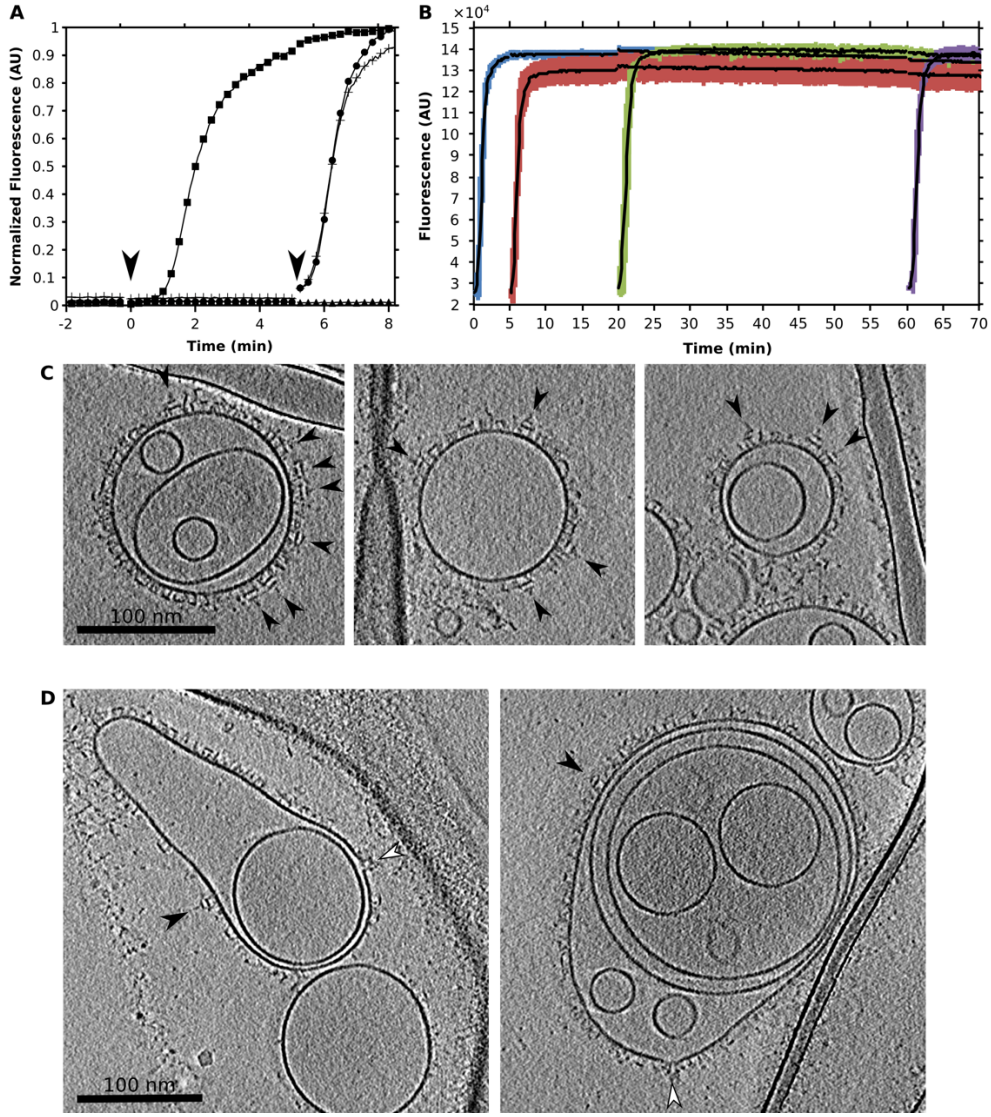

Fig. S2. Complement activation by IgM is inhibited at 4°C.

A) Increase in fluorescence caused by sulforhodamine B release from antigenic liposomes at 21°C after complement activation mediated by IgM in the presence of normal human serum (NHS). Activation by addition of either IgM after pre-incubation of liposomes with NHS (■), after addition of NHS to liposomes at time = 0 (**+**), or NHS after addition of IgM to liposomes at time = 0 (●) occurred at the timepoint indicated with arrowheads. Liposomes and IgM alone (▲) did not lyse liposomes. **B)** Antigenic liposomes pre-opsonized with IgM were incubated with NHS on ice until assay at the timepoints indicated. Samples were kept on ice for 0 min (blue), 5 min (red), 20 min (green) and 60 min (purple). Black lines are averages and error bars are standard deviations for n=3 independent measurements for each timepoint. **C)** Tomographic slices through phase-plate cryo-electron tomograms of antigenic-liposomes opsonized with IgM and incubated at 4°C with NHS for 20 min before vitrification. **D)** Tomographic slices through phase-plate cryo-electron tomograms of antigenic-liposomes opsonized with IgM and incubated at 4°C with NHS for 20 min before being incubated at 21°C for a further 20 min before vitrification. Black arrowheads indicate IgM-C1 complexes. White arrowheads indicate membrane-attack complex (MAC) pores.

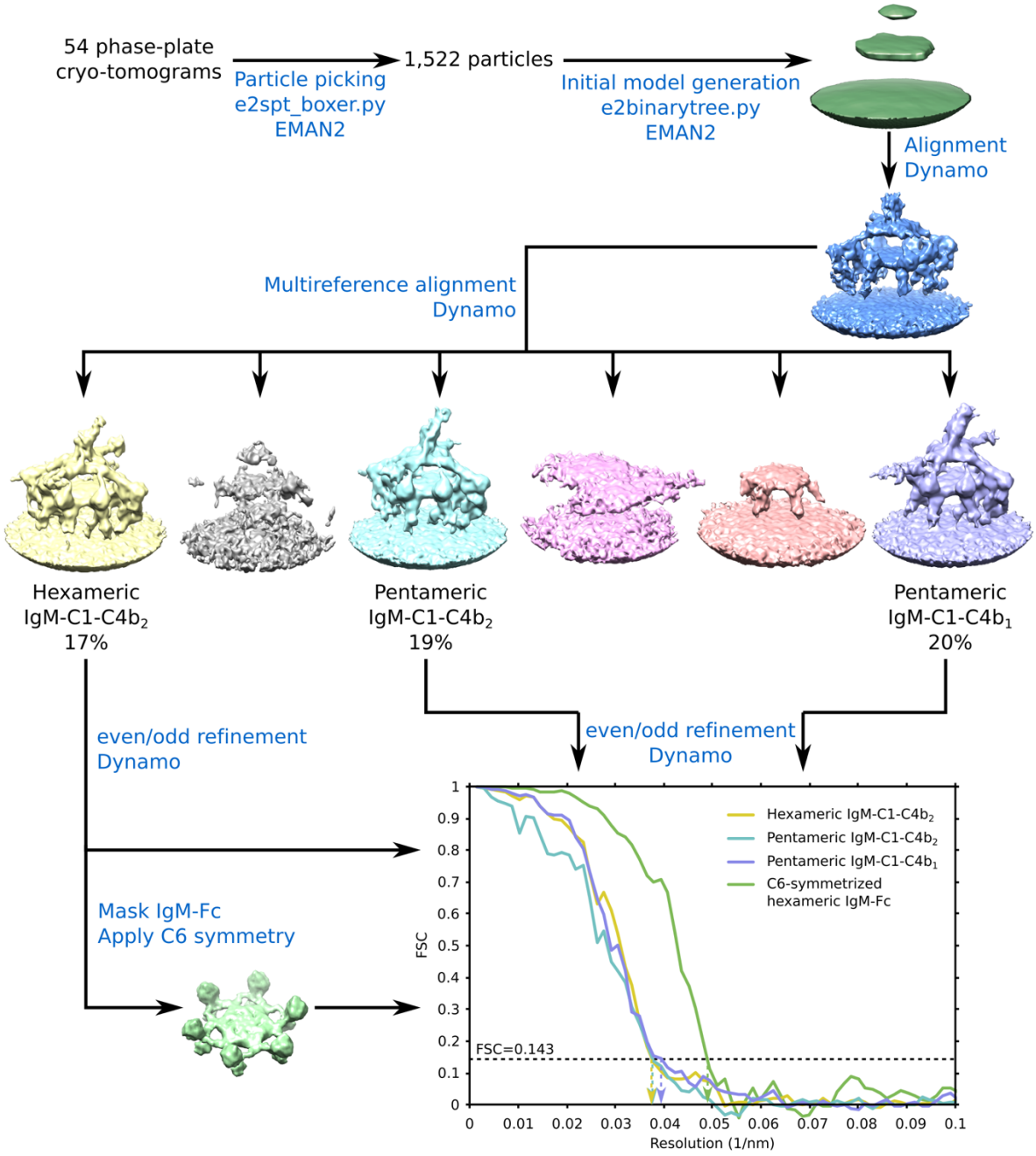

Fig. S3. Subtomogram averaging and classification scheme and FSC curves.
The initial model and reference for multireference alignment classification are shown as green and blue surfaces, resp. The resulting classes are shown below, of which three, hexameric IgM-C1-C4b2 (yellow), pentameric IgM-C1-C4b2 (cyan) and pentameric IgM-C1-C4b1 (purple) were subject to even-odd refinement following gold-standard procedures (18), yielding overall final resolutions of 26.7 Å for the hexameric IgM-C1-C4b2 complex, 26.6 Å for the pentameric IgM-C1-C4b2 complex, and 25.6 Å for the pentameric IgM-C1-C4b1 complex. After even-odd refinement, the Fc-platform of hexameric IgM-C1-C4b2 complex was masked and C6 symmetry applied to yield a map at 20.4 Å (light green). Resolutions reported at FSC = 0.143. See Materials and Methods for more information.

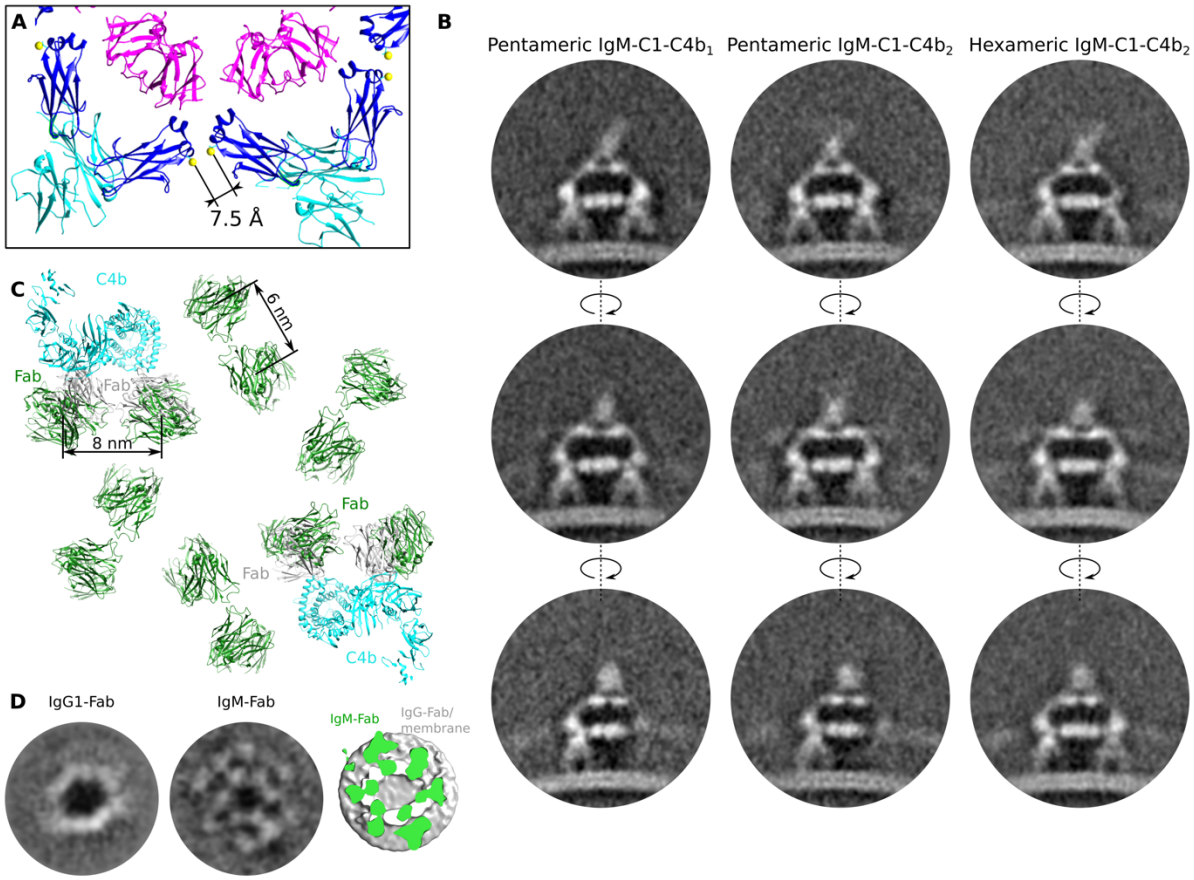

Fig. S4. Analysis of hexameric and pentameric IgM complexes.
A) The sulfur atoms (yellow spheres) mediating IgM oligomerisation of Cμ3 and Cμ3' Cys414 residues are separated by 7.5 Å. Cμ3 and Cμ4 are shown as blue and purple ribbons, respectively. **B)** Slices through tomographic volumes of pentameric IgM-C1-C4b1 (*left*), pentameric IgM-C1-C4b2 (*middle*), and hexameric IgM-C1-C4b2 (*right*) complexes showing two bound Fab regions per IgM monomer. **C)** Fab domains adjacent to the C4b region (cyan) were moved from their C6-symmetric position (grey) to better fit the density (green). Distances were measured between residues Y532 of each Fab. **D)** Alignment of subtomogram averages of IgG (19) (*left* and grey surface) and IgM (*middle* and green surface) reveals the Fab domains from IgG correspond most closely to those of the inner ring of IgM-Fab domains.

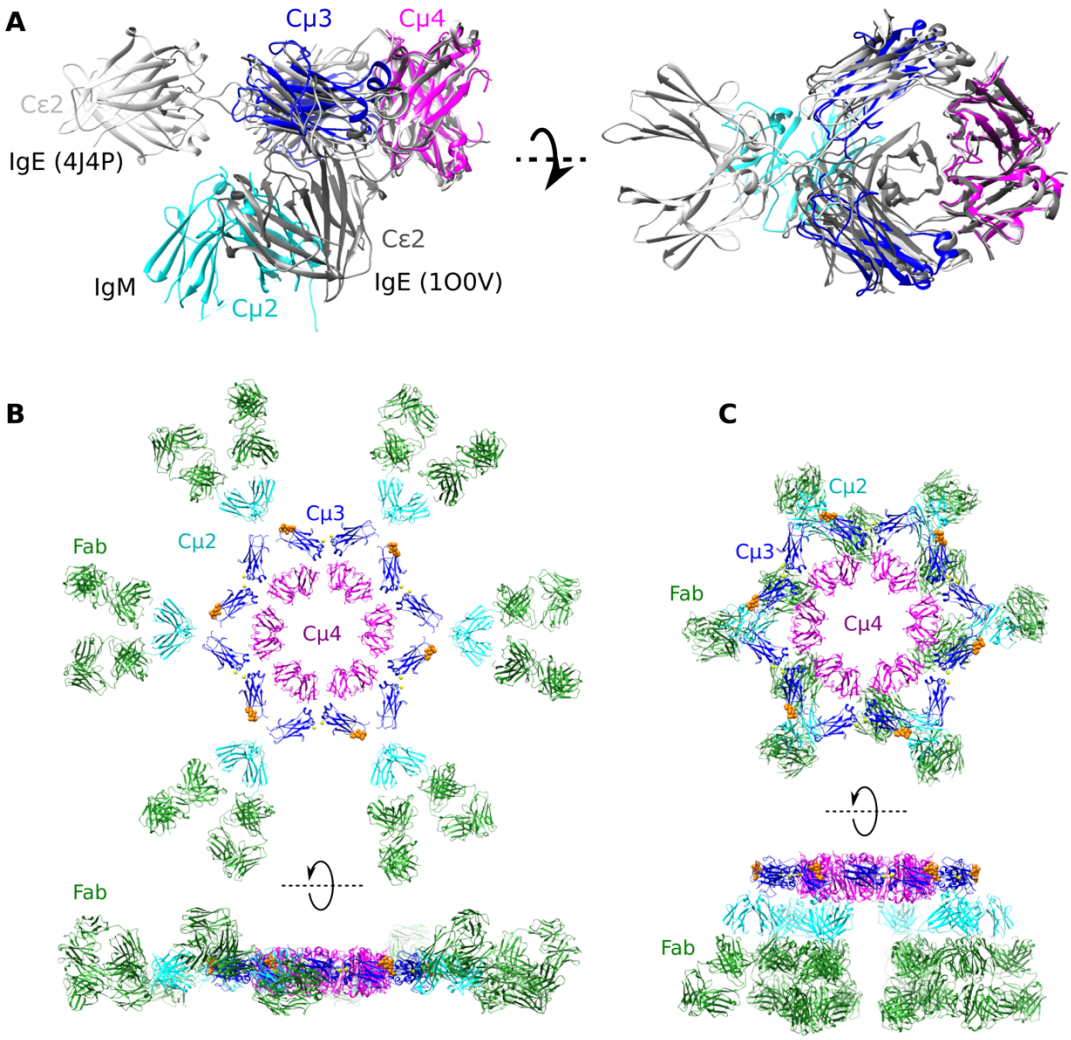

Fig. S5. Hypothetical stellate model of solution-phase IgM based on IgE crystal structures. **A)** Crystal structures of IgE in a tightly-kinked (7) (dark grey, pdb code 1O0V) and fully extended (20) (light grey, 4J4P) conformation overlaid with IgM (colored models, with Cμ4 in purple, Cμ3 in blue, Cμ2 in cyan). **B)** Aligning the fully-extended IgE structure with separate IgM Cμ3/4 and Cμ2 models yields a hypothetical model of stellate hexameric IgM. **C)** Model of antigen-bound hexameric IgM for comparison with (B). Coloring for (B) and (C): purple, Cμ4 dimers (5) (pdb code 4JVW); blue Cμ3 domains (5) (4BA8); light blue, Cμ2 domains (5) (4JVU); green, Fab domains (9) (1DEE); orange spheres, DLPSP residues mediating C1q binding.

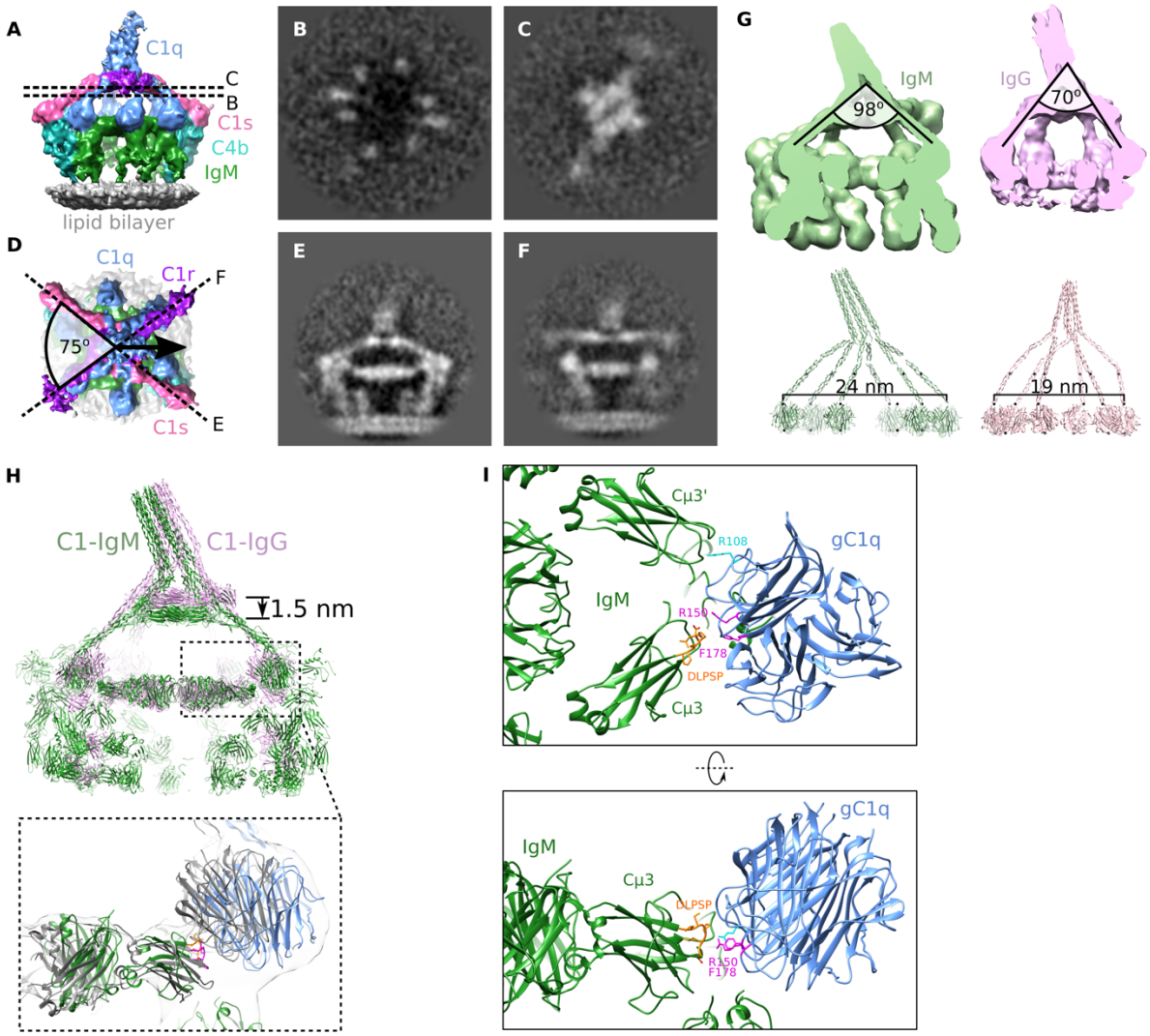

Fig. S6. Analysis of C1 bound to hexameric IgM.

A-C) Slices through the subtomogram average at the regions indicated in (A) show six collagen legs arranged as the points of a hexagon and two additional densities corresponding to C1s-CCP domains (B), and the C1rs platform (C) displaying approximate C2-symmetry. **D-F)** Slices through the subtomogram average at the regions indicated in (D) show the C1s (E) and C1r (F) arms extending from the C1rs platform. The C1r and C1s arms are separated by ~75° around the z-axis (perpendicular to the membrane) with the C1q stalk tilting halfway between them. **G)** Analysis of the angles between the collagen helices and the gC1q head domains of both IgM (green) and IgG (pink), and the distance between gC1q units. **H)** Comparison of C1 models in complex with IgG (pink) and IgM (green) shows the 1.5 nm difference in height at the C1rs platform and a similar tilted C1q stalk. Inset shows the side view of C1 bound to IgM (colored models) and IgG (grey models) indicating a relative rotation of gC1q modules, associated with spreading of C1q collagen helices. **I)** Analysis of gC1q (blue) binding to the IgM DLPSP residues (orange) of Cμ3. Potential interactions are shown between the C1q-B chain residues R^{B108} (cyan) with the Cμ3' BC loop, and R^{B150} and F^{B178} (purple) with Cμ3 DLPSP residues (orange).

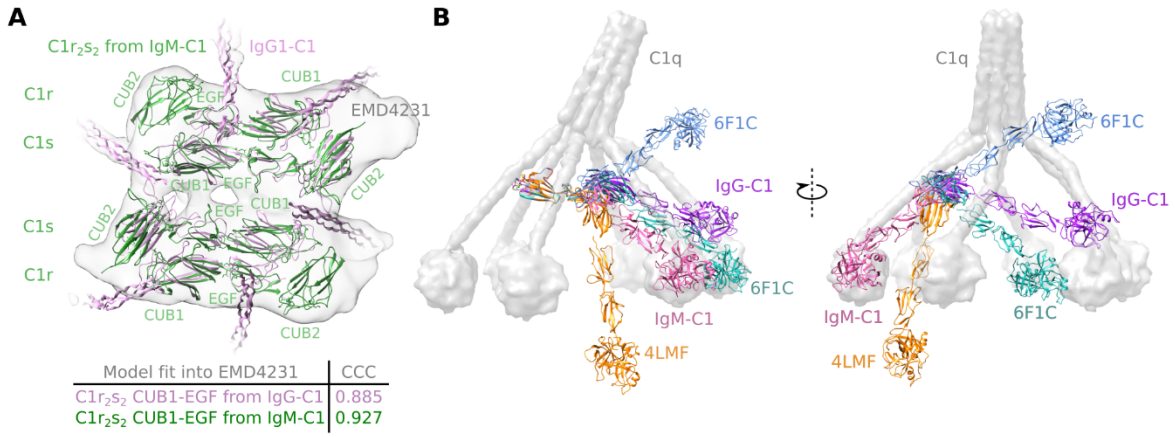

Fig. S7. Analysis of $C1r_2s_2$ platform domains.

A) The arrangement of C1rs CUB1-EGF-CUB2 domains as determined in the hexameric IgM-C1-$C4b_2$ map (green) fit into the map of the IgG1-C1 complex (19) (grey). Compared to the model from Ugurlar *et al.* (19) (pink), the CUB1-EGF domains fit with a higher cross-correlation coefficient (CCC). **B)** The varied orientations of the C1s CUB2 domain, as found in crystal structures 6F1C (12), 4LMF (21), models of C1 bound to IgG (19) and the IgM-C1-C4b complexes demonstrates the structural variability of the C1s protease arm.

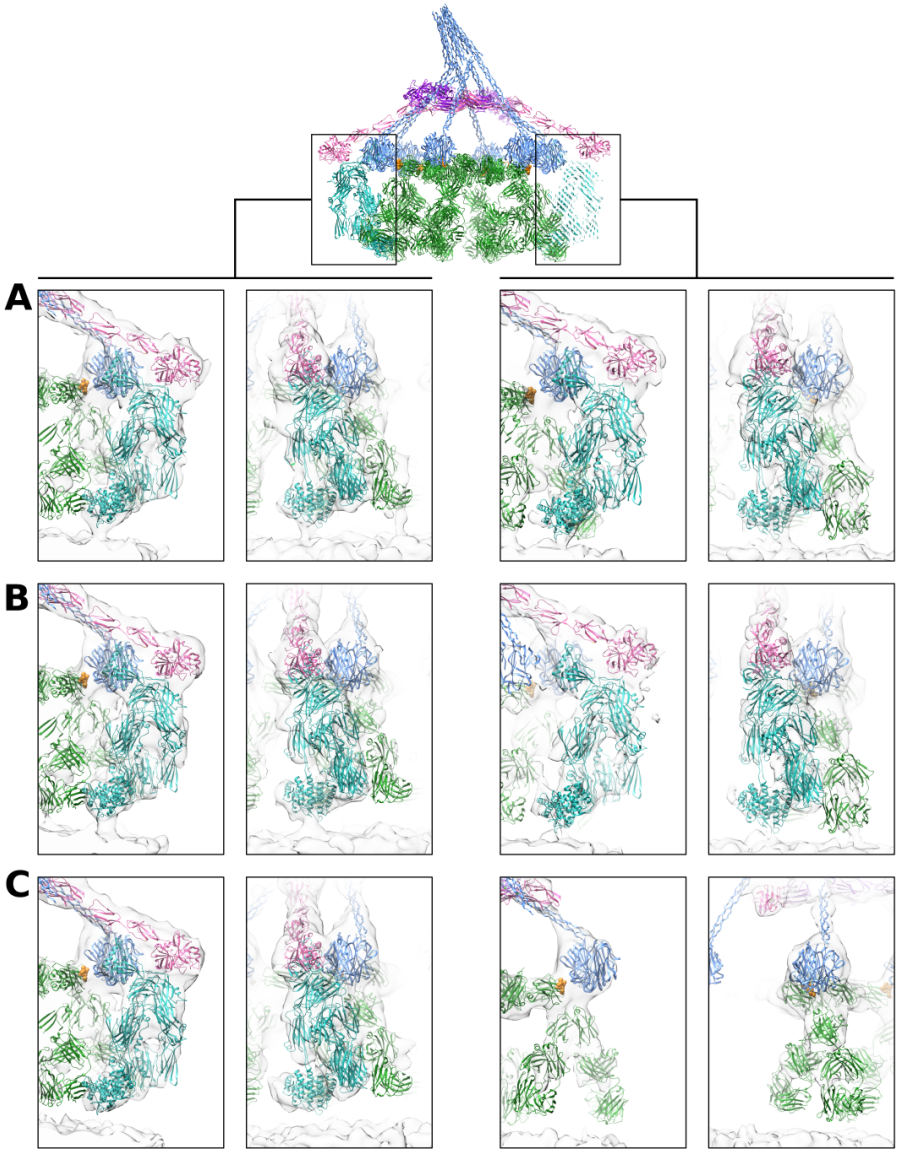

Fig. S8. Hexameric and pentameric IgM-C1 complexes bind to one or two C4b molecules. A-C), Density corresponding to C4b is consistently more defined on the side which the C1q stalk is tilted towards. C4b bound to the hexameric IgM-C1-C4b$_2$ complex (A), the pentameric IgM-C1-C4b$_2$ complex (B), and the pentameric IgM-C1-C4b$_1$ complex (C). C1q, blue; C4b, cyan; C1s, pink; IgM, green; DLPSP-residues, orange.

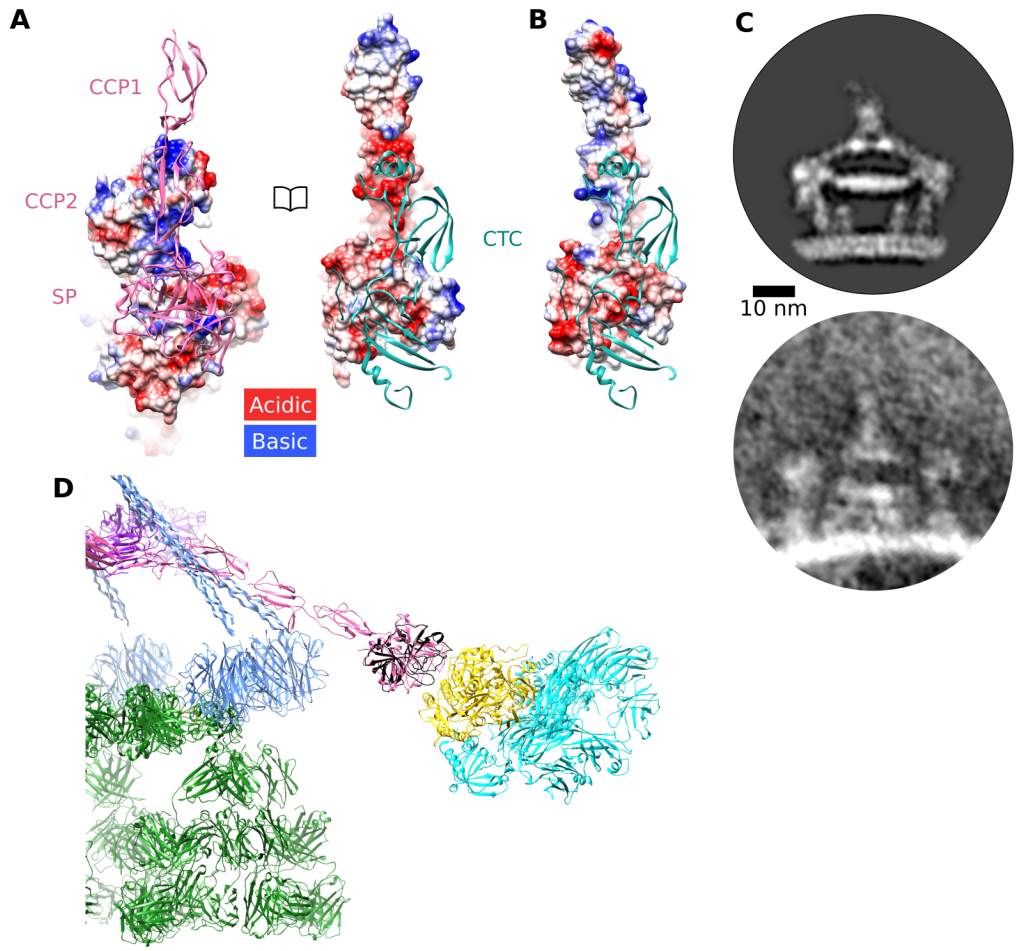

Fig. S9. Interactions of C1 and IgM with C4b.
A) Electrostatic interactions described for the homologous MASP2-C4b interaction (15) are also present in this C1s-C4b model. C1s is shown as pink ribbons, C4b is shown as cyan ribbons. The basic (blue) CTC domain of C4b is adjacent to the acidic C1s-CCP exosite. **B)** The C1r-CCP exosite does not contain highly charged residues, minimizing potential electrostatic interactions with C4b. **C)** Comparison of the hexameric IgM-C1-C4b2 average (top) with an individual observation of a potential IgG-C1-C4b complex (22) (bottom). **D)** A hypothetical structure of C4bC2 bound to C1s formed by aligning factor D (black) from the crystal structure of C3bBD (23) to the C1s SP domain (pink) shows that additional changes in the orientation of the C1s SP domain is needed to cleave C4bC2 into the (C4b2a) C3 convertase.

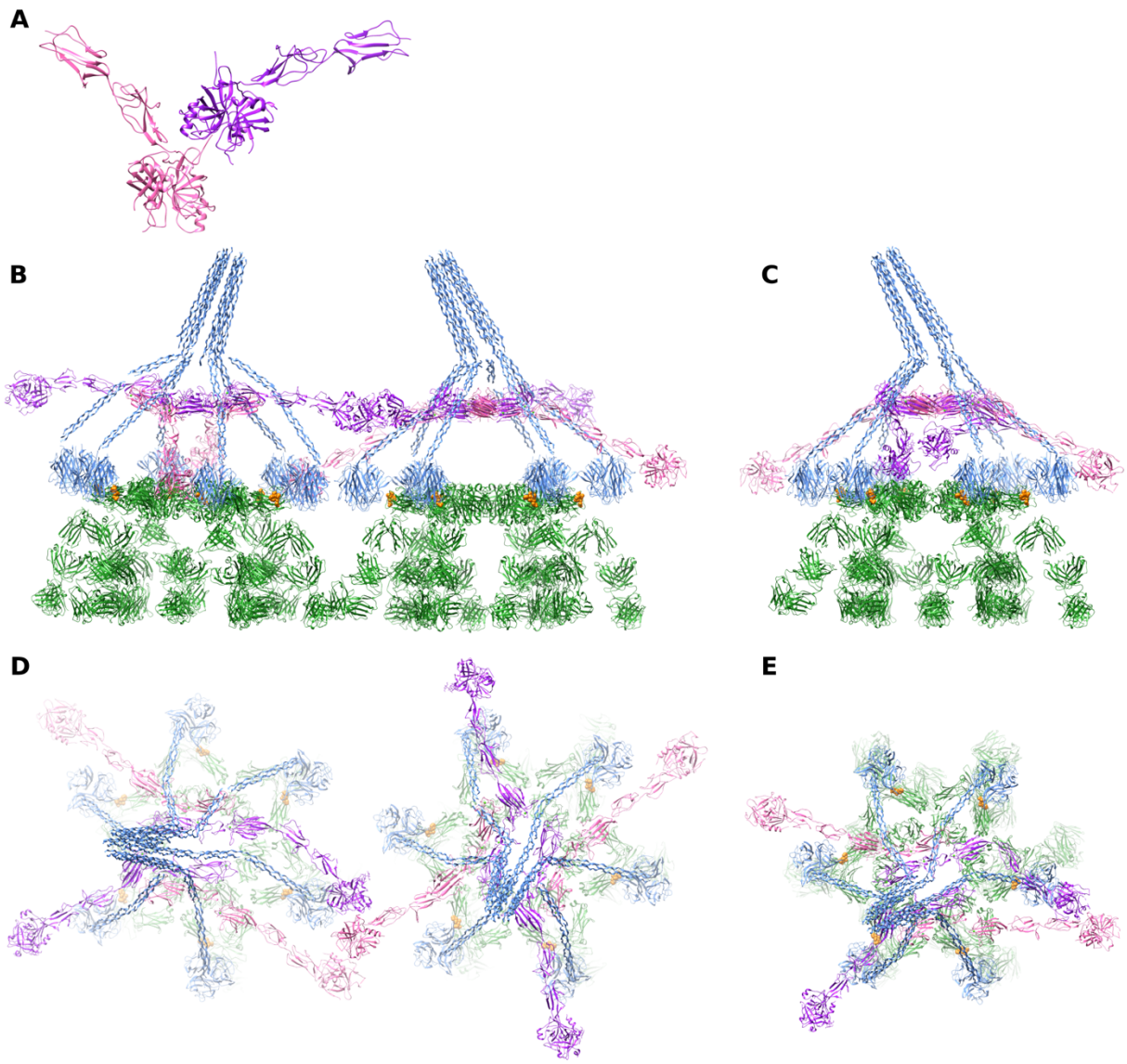

Fig. S10. Potential C1r activation models.
A) Crystal structure of C1r in an enzyme (purple)-product (pink) arrangement (24) (pdb code 2QY0). **B)** Intermolecular activation of C1r (purple) in adjacent complexes requires flexibility around the CUB2-CCP1 interface. **C)** Intramolecular autoactivation of C1r requires a sharp kink in the region of CUB2-CCP1. **D)** C1r (purple) activating C1s (pink) of an adjacent complex. **E)** C1r activating C1s of the adjacent C1rs heterodimer within the same C1 complex.

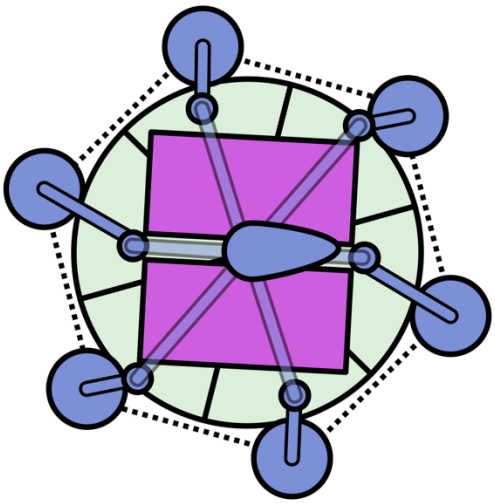

Movie S1. Movie showing a schematic representation of the conformational rearrangements of the C1 complex upon binding to antibody-Fc platforms; with C1q (blue), C1rs heterodimers (purple) and antibodies (green). Empty sites for antibody binding are indicated in grey, C1q positions at the height of the proteases by small blue circles, gC1q headpieces by large blue circles, connecting C1q collagen helices by blue bars, and upright and tilted C1q stalks as a blue circle or ovoid. Dotted lines highlight the hexagonal arrangements. The sliding motion of two halves of the complex is indicated by the colored arrow. See also **Fig 3.**

Protein	Domain(s)	PDB code	Reference
IgM	Fab	1DEE	(9)
	Cμ2	4JVU	(5)
	Cμ3	4BA8	(5)
	Cμ4	4JVW	(5)
C1q	Globular head	1PK6	(11)
	Collagen arms	-	(10)
C1r	CUB1-EGF-CUB2	6F1C	(12)
	CCP1-CCP2-SP	1GPZ	(13)
C1s	CUB1-EGF-CUB2	6F1C	(12)
	CCP1-CCP2-SP	4J1Y	(14)
C4b	-	5JTW	(16)

Table S1. Summary of crystal structures and models used in the final model of IgM-C1-C4b.

Supplementary references

1. Danev R, Buijsse B, Khoshouei M, Plitzko JM, & Baumeister W (2014) Volta potential phase plate for in-focus phase contrast transmission electron microscopy. *Proc Natl Acad Sci U S A* 111(44):15635-15640.
2. Kremer JR, Mastronarde DN, & McIntosh JR (1996) Computer visualization of three-dimensional image data using IMOD. *J Struct Biol* 116(1):71-76.
3. Galaz-Montoya JG, Flanagan J, Schmid MF, & Ludtke SJ (2015) Single particle tomography in EMAN2. *J Struct Biol* 190(3):279-290.
4. Castano-Diez D, Kudryashev M, Arheit M, & Stahlberg H (2012) Dynamo: a flexible, user-friendly development tool for subtomogram averaging of cryo-EM data in high-performance computing environments. *J Struct Biol* 178(2):139-151.
5. Muller R*, et al.* (2013) High-resolution structures of the IgM Fc domains reveal principles of its hexamer formation. *Proc Natl Acad Sci U S A* 110(25):10183-10188.
6. Czajkowsky DM & Shao Z (2009) The human IgM pentamer is a mushroom-shaped molecule with a flexural bias. *Proc Natl Acad Sci U S A* 106(35):14960-14965.
7. Wan T*, et al.* (2002) The crystal structure of IgE Fc reveals an asymmetrically bent conformation. *Nat Immunol* 3(7):681-686.
8. Pettersen EF*, et al.* (2004) UCSF Chimera--a visualization system for exploratory research and analysis. *J Comput Chem* 25(13):1605-1612.
9. Graille M*, et al.* (2000) Crystal structure of a Staphylococcus aureus protein A domain complexed with the Fab fragment of a human IgM antibody: structural basis for recognition of B-cell receptors and superantigen activity. *Proc Natl Acad Sci U S A* 97(10):5399-5404.
10. Wood CW & Woolfson DN (2018) CCBuilder 2.0: Powerful and accessible coiled-coil modeling. *Protein Sci* 27(1):103-111.
11. Gaboriaud C*, et al.* (2003) The crystal structure of the globular head of complement protein C1q provides a basis for its versatile recognition properties. *J Biol Chem* 278(47):46974-46982.
12. Almitairi JOM*, et al.* (2018) Structure of the C1r-C1s interaction of the C1 complex of complement activation. *Proc Natl Acad Sci U S A* 115(4):768-773.
13. Budayova-Spano M*, et al.* (2002) The crystal structure of the zymogen catalytic domain of complement protease C1r reveals that a disruptive mechanical stress is required to trigger activation of the C1 complex. *EMBO J* 21(3):231-239.
14. Perry AJ*, et al.* (2013) A molecular switch governs the interaction between the human complement protease C1s and its substrate, complement C4. *J Biol Chem* 288(22):15821-15829.
15. Kidmose RT*, et al.* (2012) Structural basis for activation of the complement system by component C4 cleavage. *Proc Natl Acad Sci U S A* 109(38):15425-15430.
16. Mortensen S*, et al.* (2015) Structural Basis for the Function of Complement Component C4 within the Classical and Lectin Pathways of Complement. *J Immunol* 194(11):5488-5496.
17. Croll TI & Andersen GR (2016) Re-evaluation of low-resolution crystal structures via interactive molecular-dynamics flexible fitting (iMDFF): a case study in complement C4. *Acta Crystallogr D Struct Biol* 72(Pt 9):1006-1016.
18. Henderson R*, et al.* (2012) Outcome of the first electron microscopy validation task force meeting. *Structure* 20(2):205-214.

19. Ugurlar D*, et al.* (2018) Structures of C1-IgG1 provide insights into how danger pattern recognition activates complement. *Science* 359(6377):794-797.
20. Drinkwater N*, et al.* (2014) Human immunoglobulin E flexes between acutely bent and extended conformations. *Nat Struct Mol Biol* 21(4):397-404.
21. Venkatraman Girija U*, et al.* (2013) Structural basis of the C1q/C1s interaction and its central role in assembly of the C1 complex of complement activation. *Proc Natl Acad Sci U S A* 110(34):13916-13920.
22. Sharp TH, Faas FG, Koster AJ, & Gros P (2017) Imaging complement by phase-plate cryo-electron tomography from initiation to pore formation. *J Struct Biol* 197(2):155-162.
23. Forneris F*, et al.* (2010) Structures of C3b in complex with factors B and D give insight into complement convertase formation. *Science* 330(6012):1816-1820.
24. Kardos J*, et al.* (2008) Revisiting the mechanism of the autoactivation of the complement protease C1r in the C1 complex: structure of the active catalytic region of C1r. *Mol Immunol* 45(6):1752-1760.